Nanoscale

Antiferromagnetic Proximity Coupling between Semiconductor Quantum Emitters in WSe2 and van der Waals Ferromagnets

Journal:	*Nanoscale*
Manuscript ID	NR-ART-09-2020-006632.R1
Article Type:	Paper
Date Submitted by the Author:	08-Dec-2020
Complete List of Authors:	Liu, Na; Stevens Institute of Technology, Physics Gallaro, Cosmo; Stevens Institute of Technology, Physics Shayan, Kamran; University of Rochester, The Institute of Optics Mukherjee, Arunabh; University of Rochester, The Institute of Optics Kim, Bumho; Columbia University, Mechanical Engineering Hone, James; Columbia University, Mechanical Engineering Vamivakas, Nick; University of Rochester, The Institute of Optics Strauf, Stefan; Stevens Institute of Technology, Physics

Antiferromagnetic Proximity Coupling between Semiconductor Quantum Emitters in WSe_2 and van der Waals Ferromagnets

Na Liu[1,2], Cosmo M. Gallaro[1,2], Kamran Shayan[3,4], Arunabh Mukherjee[3,4], Bumho Kim[5], James Hone[5], Nick Vamivakas[3,4,6], Stefan Strauf[1,2]*

[1]Department of Physics, Stevens Institute of Technology, Hoboken, New Jersey 07030, United States.

[2]Center for Quantum Science and Engineering, Stevens Institute of Technology, Hoboken, New Jersey 07030, United States

[3]The Institute of Optics, University of Rochester, Rochester, New York 14627, United States.

[4]Center for Coherence and Quantum Optics, University of Rochester, Rochester, New York 14627, United States.

[5]Department of Mechanical Engineering, Columbia University, New York 10027, United States.

[6]Department of Physics and Astronomy, University of Rochester, Rochester, New York 14627, United States.

*Address correspondence to: sstrauf@stevens.edu

Abstract

Van der Waals ferromagnets have gained significant interest due to their unique ability to provide magnetic response even at the level of a few monolayers. Particularly in combination with 2D semiconductors, such as the transition metal dichalcogenide WSe_2, one can create heterostructures that feature unique magneto-optical response in the exciton emission through the magnetic proximity effect. Here we use 0D quantum emitters in WSe_2 to probe for the ferromagnetic response in heterostructures with Fe_3GT and Fe_5GT ferromagnets through an all-optical read-out technique that does not require electrodes. The spectrally narrow spin-doublet of the WSe_2 quantum emitters allowed to fully resolve the hysteretic magneto-response in the exciton emission, revealing the characteristic signature of both ferro- and antiferromagnetic proximity coupling that originates from the interplay among Fe_3GT or Fe_5GT, a thin surface oxide, and the spin doublets of the quantum emitters. Our work highlights the utility of 0D quantum emitters for probing interface magnetic dipoles in vdW heterostructures with high precision. The observed hysteretic magneto response in the exciton emission of quantum emitters adds further new degrees of freedom for spin and g-factor manipulation of quantum states.

Introduction

Two dimensional (2D) van der Waals (vdW) ferromagnets have been shown to demonstrate extreme usefulness due to their sensitivity to external magnetic fields, spin dynamics, and charge transport characteristics[1]. They can also be layered with graphene, hexagonal boron nitride (hBN), or 2D semiconductors such as transition metal dichalcogenide (TMDC) monolayers via the magnetic proximity effect, thereby creating heterostructures with novel magneto-optical and electronic properties[2,3], such as three-state asymmetric magnetoresistance[4], twist-angle dependent proximity exchange[5], or near-ideal tunneling spin valves[6]. TMDC monolayers feature strong spin-orbit coupling and an intrinsic inversion symmetry breaking that results in valley degeneracy at the K and K' points[7,8]. Application of external magnetic fields gives rise to a lifting of the valley degeneracy and opportunities for optical spin/valley manipulation. These valleytronic effects can be probed through the circularly polarized light emission of excitons within 2D TMDC[9]. When TMDC form heterostructures with vdW ferromagnets, pronounced proximity-coupling can occur, as was recently demonstrated via spin-valley polarization signatures in the optical response of 2D neutral excitons residing in EuS/WSe_2[10], EuO/ $MoTe_2$[11], and CrI_3/WSe_2[12].

The magnetic properties of vdW materials themselves can be manipulated through the thickness[13,14], atomic composition[15,16], and applied gating bias[17,18], offering a tremendous versatility for on-chip applications. Specifically, ferromagnetic vdW compounds such as CrI_3[13,19,20], Cr_2GeTe_2 (CGT)[21] and Fe_3GeTe_2 (Fe_3GT)[1,22] display different degrees of ferromagnetism. For example, CGT exhibits soft ferromagnetism, i.e., a very narrow hysteresis loop that can hardly be resolved experimentally, as well as a relatively high magnetization of $3\mu_B$[23]. In contrast, Fe_3GT is a ferromagnetic metallic single-layer material[24] that exhibits hard ferromagnetism, giving rise to a very pronounced hysteresis loop[14] as well as a relatively high ferromagnetic Tc ranging from 150 K to 230 K depending on Fe occupancy[15,24,25]. Recent studies have shown that the Tc of Fe_3GT can reach even room temperature through external manipulation, such as a control of gate bias[17], or micro structuring of Fe_3GT[26]. Furthermore, crystals of Fe_5GeTe_2 (Fe_5GT) are of interest since they display a Curie temperature approaching room temperature even without external gate biasing, due to their high Fe atom concentration[27,28].

When exfoliated into thinner layers it was discovered in cross-sectional transmission electron microscope images that air exposed Fe_3GT forms a native oxide within a few minutes[14]. This amorphous oxide layer transforms the magnetic interaction from ferromagnetic to an antiferromagnet response[29]. Antiferromagnetism is a state where the ordered neighboring dipole spins point in opposite directions. Despite the notorious difficulty in using antiferromagnets due to their net vanishing magnetization, they hold great promise for high-speed, low power spintronics because they have magnetic resonance frequencies in the terahertz regime as well as robustness against external magnetic field perturbation[30,31]. Furthermore, antiferromagnets are much more abundant than ferromagnets[3]. They can also be engineered into layered heterostructures. For example, CrI_3 bilayer exhibit layered antiferromagnetism, in which adjacent ferromagnetic monolayers are antiferromagnetically coupled[13]. Remarkably, recent theory predicts that it is possible to use injected current pulses to reversibly induce phase transitions between ferromagnetic and antiferromagnetic response in heterostructures of $TaSe_2$ with bilayer CrI_3[32].

To probe the underlying interface magnetism recent advances utilized monolayer WSe_2 as a spatially sensitive magnetic sensor to map out layered antiferromagnetic domains[33]. By introducing an insulating oxide-based spacer layer of a few nm thickness it is also possible to probe for antiferromagnetic interlayer exchange coupling (AF-IEC) between ferromagnetic layers, thereby engineering materials through layering stacks with opposite spin directions[34]. The AF-IEC in these correlated-oxide multilayers can be treated as a composite material with net antiferromagnetic properties. Another appealing technique to probe the local magnetic field in 2D vdW magnets is based on magnetometry with single quantum emitters. In this way room temperature ferromagnetism was confirmed for in situ Fe-doped MoS_2 with a local field up to 0.5 mT[35]. Likewise, 0D exciton quantum emitters offer significantly higher spectral resolution than common

2D exciton transitions that suffer from spectrally broad linewidth, leading to higher magnetic field sensitivity. Using the spin doublets of quantum emitters in WSe_2 we have recently shown that magnetic proximity-coupling with CGT vdW layers can give rise to drastically enhanced exciton g-factors up to 20, i.e., a three-fold enhanced magnetic response[36]. However, the soft ferromagnetism of CGT has prevented so far, the observation of magnetic hysteresis effects in the magneto-response of quantum emitters, while coupling to vdW hard ferromagnets is entirely unexplored.

Here we utilize quantum emitters in WSe_2 to probe for the ferromagnetic response in heterostructures with Fe_3GT and Fe_5GT through an all-optical read-out technique. The spectrally narrow spin-doublet of the WSe_2 quantum emitters allows to fully resolve the hysteretic magneto-response in the exciton emission. The magnetic field sweeps demonstrate the characteristic features of an antiferromagnetic proximity coupling effect through the vortex reversal shapes up to the saturation field. The antiferromagnetic response originates in the interplay among Fe_3GT or Fe_5GT, a thin surface oxide layer, and the exciton spin doublets within the investigated heterostructures. In contrast, the response renders into a symmetric hysteresis loop as expected for ferromagnetic proximity coupling in the absence of the oxide layer for samples made inside a glove box. We further provide a qualitative model that gives insights into the switching between coupled and uncoupled spin orientations between the quantum emitters and the antiferromagnetic vdW layers.

Results and discussions

With the goal to investigate magnetic proximity coupling for quantum emitters in WSe_2 monolayers, we have utilized three different vdW ferromagnetic materials that are known to either display soft-ferromagnetism (CGT) or hard-ferromagnetism (Fe_3GT and Fe_5GT). **Figures 1a-1c** show the top down view of the schematic crystal structure of CGT, Fe_3GT and Fe_5GT, respectively. In the CGT structure shown in **Fig. 1a** the Cr atoms form a 2D honeycomb spin arrangement, where each Cr atom binds with six Te atoms in an octahedral crystal environment. Bulk CGT has a layered structure with an interlayer vdW spacing of 3.4 Å[21,37]. Fe_3GT crystallizes as a hexagonal layered structure with space group $P6_3/mmc$ (No. 194)[17,31]. **Figure 1b** illustrates the structure as a nanosheet of bulk Fe_3GT, where each layer consists of covalently bonded Fe-Ge heterometallic slabs being sandwiched between two Te layers[17]. The partially filled d orbitals of Fe dominate the band structure around the Fermi level, giving rise to itinerant ferromagnetism in bulk Fe_3GT. Adjacent monolayers are separated by a 2.95Å van der Waals gap in the bulk crystal[38]. Likewise, the structure of Fe_5GT (**Fig. 1c**) is made up of two-dimensional slabs of Fe and Ge between layers of Te. The difference is in the sections between the Te layers where the building blocks consist of alternating layers built up by Fe-Ge and Fe-Fe hexagons[28,39]. As a result, there are two iron atoms in a unit cell of Fe_5GT, in comparison to one atom of iron per Fe_3GT unit cell, as illustrated by the dashed lines in **Fig.1b** and **1c.** The exfoliated vdW ferromagnetic layers are produced in air by means of a cold stamping and hard pressing transfer technique onto a 285nm SiO_2 substrate (see methods). Crystal thickness was determined from atomic force microscope images resulting in 55 nm for CGT, 150 nm for Fe_3GT, and 100 nm for Fe_5GT (**Supplementary Figure 1**). These values imply bulk ferromagnetic properties, e.g. the Curie temperature does not change for crystal thickness between 50 nm and several microns[14]. Subsequently, monolayers of WSe_2 have been transferred on top of the ferromagnetic multilayers by the same method. As we have reported before, this approach gives rise to nanobubble formation in the monolayer WSe_2 that creates strain-induced 0D quantum emitters at randomized spatial locations[40]. The top down view of the assembled heterostructure of CGT/WSe_2 is shown **Fig. 1d**, for Fe_3GT/WSe_2 in **Fig. 1e** and for Fe_5GT/WSe_2 in **Fig. 1f**. Note that we observe a surface darkening effect that occurs for Fe_3GT containing heterostructures only after prolonged storage of six months, but for heterostructures formed with thin layers (< 100 nm) of Fe_5GT already within seconds during the exfoliation process (see **Supplementary Figure 2**). The darkening is accompanied with a reduced intensity from the quantum emitters and thus detrimental for

optical magnetometry. For the case of Fe_5GT the surface darkening can be mitigated by utilizing relatively thick layers (≥100 nm) to form heterostructures, for which we do not observe surface darkening during the measurement process. In the following we only report results from "fresh samples" that do not suffer from surface darkening effects.

To characterize the exciton emission, we carried out hyperspectral micro-photoluminescence (μ-PL) imaging of the fabricated heterostructures as shown in **Figs. 2a-2c** (see methods). **Figure 2d** displays an exemplary PL spectrum from a specific location which includes 2D neutral excitons (2D-X^0) in the 710 nm wavelength area and the defect band exciton emission (DBX) occurring in the wavelength range from 720 to 780 nm. These peaks are in accordance with previous reports of photoluminescence from monolayer WSe_2 [7,41]. The appearance of well separated and spectrally sharp emission lines below the ensemble emission of the DBX emission is a characteristic feature of trapped nanobubbles in the WSe_2 monolayer that create strain-induced 0D quantum emitters[40]. To provide more insight into the exciton emission properties, we utilized 2D hyperspectral imaging to address each excitonic species separately. **Figure 2a** shows the scan for the 2D-X^0 emission with a 10 nm band pass filter centered at 710 nm resulting in a rather uniform distribution that reproduces the outline of the WSe_2 monolayer region. **Figure 2b** shows the scan of the DBX emission filtered around 730 nm. In this region typically many sharp lines merge into a broader continuum characteristic of the ensemble emission of the 0D quantum emitters, thereby producing a rather uniform distribution in the spatial scans. Additionally, the trion emission occurs typically around 720 nm in our WSe_2 samples[40], as well as the 2D dark exciton emission centered around 734 nm[42], which are both uniformly distributed. In contrast, the sharp peak at 770 nm appears as a strongly localized emission in **Fig. 2c**, which is characteristic for strain-induced 0D quantum emitters and helps to quickly identify them. In the following we focus only on the emission of these strongly localized 0D exciton emission centers if they appear spectrally well separated from other uniformly distributed emission bands, in order to probe for magnetic proximity coupling, which can occur anywhere in the wavelength range from 720 – 780 nm[41,42].

Another characteristic feature of these 0D quantum emitters is their fine structure splitting (FSS) at zero magnetic field. All investigated quantum emitters display spectral doublets when recorded with high spectral resolution with a typical FSS energy Δ_0=500-800 μeV[36]. To investigate the magneto-PL properties of each 0D quantum emitter, we applied the magnetic field parallel to the k vector of the incident laser. **Figure 2e** shows the magnetic field dependence of an exemplary quantum emitter with a Δ_0 of 571μeV that originates from the electron-hole spin exchange interaction as well as the underlying anisotropic strain, which also causes the low-energy peak of the doublet to dominate the spectrum[43,44]. With an increasing applied magnetic field, B, the two components of the clearly resolved Zeeman doublet split further apart. The doublet's splitting behavior with increasing magnetic fields up to 9 T is shown in **Fig. 2f**. The Zeeman splitting energy, ΔE, was analyzed to determine the g factor using the relation $\Delta E = \sqrt{\Delta_0^2 + (g\mu_0 B)^2}$, where μ_0 is the Bohr magneton and g is the exciton g factor, revealing g=6.2±0.5. This g factor is in good agreement with recent reports of quantum emitters in WSe_2 monolayers[36,42]. Note we excluded the occasional occurrence of quantum emitters that display a nonmagnetic behavior from this study, which are characterized by a single sharp peak with no zero-field splitting and no spectral response even at a 9 T magnetic field.

Figure 3 compares the ferromagnetic hysteresis behavior for increasing and decreasing magnetic field sweeps for quantum emitters in the fabricated heterostructures between WSe_2 and the three vdW ferromagnets. The schematic representation of the heterostructure layer arrangements for CGT/WSe_2, Fe_3GT/WSe_2 and Fe_5GT/WSe_2 are shown in **Figs. 3a-3c,** respectively. We have recently shown that the g factor for quantum emitters in heterostructures with CGT is typically magnetic proximity-enhanced by

about 1.7-fold, with highest values up to g=20 for a well-coupled case[36]. Since the saturation magnetization of Fe_3GT ranges only from 1.2-1.8μ_B[25,28] compared to the 3μ_B of CGT[23], we won't expect the g factor for the quantum emitters residing in the heterostructures with Fe_3GT to have a similarly high enhancement. However, since the Fe_3GT is a hard-ferromagnetic material we do expect that the ferromagnetic hysteresis can be imprinted onto the quantum emitter via proximity coupling. To demonstrate this, **Fig. 3d** displays the energy splitting in the PL spectra in the CGT/WSe_2 emitter as a function of an increasing (red circles) and decreasing (blue squares) magnetic field from -2 T to 2 T at 3.5 K. The corresponding energy difference ΔM between the increasing and decreasing magnetic fields for quantum emitters residing in the CGT/WSe_2 heterostructure is shown in **Fig. 3g**. It is apparent that the quantum emitter in CGT/WSe_2 does not show any resolvable hysteresis behavior, which is a common property of soft-ferromagnetic materials. In strong contrast, the energy splitting of quantum emitter in Fe_3GT/WSe_2 (**Fig. 3e**) and Fe_5GT/WSe_2 (**Fig. 3f**) clearly shows pronounced hysteresis behavior in these magnetic field sweeps. Above 2 T the magnetic proximity coupling and hysteresis effects saturate, i.e. $\Delta M \sim 0$ within the error bar.

Interestingly, the energy difference ΔM for the Fe_3GT coupled emitter shows a sine-shaped curve switching from positive to negative values as well as no pronounced influence of the applied magnetic field near zero field conditions (**Fig. 3h & 3i**), which is the characteristic feature for anti-ferromagnetic coupling (**Fig. 3h**), i.e. the vortex reversal shapes up to the saturation field. While the bare Fe_3GT materials are known to be ferromagnets the occurrence of the antiferromagnetic coupling might be at first surprising. However, as stated above, the exfoliated Fe_3GT materials are prone to surface oxidization due to their large Fe content. It is well-known from recent reports that the oxide layer (O-Fe_3GT) forms naturally on top of exfoliated Fe_3GT, leading to antiferromagnetic coupling between Fe_3GT and the O-Fe_3GT layers in the electrical transport phenomena[29]. We therefore expect that this local anti-ferromagnetic field is also seen and sensed by the adjacent quantum emitters. To further quantify the strength of the magnetization field we fit the g factor data based on $\Delta E = \sqrt{\Delta_0^2 + (g\mu_0 B)^2}$ to each energy splitting from the increasing and decreasing magnetic fields, and calculate the enhancement of the g factor from the energy splitting at each field, as shown on the second y-axis in **Fig. 3h** for Fe_3GT and in **Fig. 3i** for Fe_5GT. The g factor enhancement is up to 1.5 times higher for Fe_3GT and up to 1.4 times higher for Fe_5GT. These values are in good agreement with values for the saturation magnetization (1.5 μ_B) in dynamic mean field theory calculations[45], indicating that the quantum emitters experience pronounced magnetic proximity coupling within the heterostructure.

If desired, one can also probe magnetic interfaces in vdW materials in the absence of O-Fe_3GT layers when sample fabrication is carried out under a glove box, i.e. in the absence of O_2 or H_2O. Previous electrical transport data revealed that Fe_3GT layers made in a glove box display a single hard magnetic phase with a near square-shaped ferromagnetic hysteresis loop[7]. For comparison to the data shown in **Figure 3**, we have carried out Fe_3GT/WSe_2 heterostructure fabrication in an N_2-filled glovebox (H_2O<0.5 p.p.m. and O_2~3 p.p.m.) and further capped these heterostructures with h-BN on top to avoid oxidation when loading into the cryostat (**Fig. 4a**). The corresponding optical image is shown in **Fig. 4b** together with the hysteresis loop (**Fig. 4c**) and ΔM-trace (**Fig.4d**). As expected, in the absence of O-Fe_3GT layers the optical response of the proximity-coupled quantum emitter is fully symmetric, and importantly, displays hard ferromagnetic properties even in the absence of an external magnetic field (B=0), which is the typical characteristic of a ferromagnet. In both cases, with and without the formation of O-Fe_3GT layers, the pronounced asymmetric or symmetric hysteretic response in the optical properties of an adjacent quantum emitter residing in monolayer WSe_2 clearly shows the underlying presence of magnetic-proximity coupling.

To gain further insights into the coupling mechanism in the presence of O-Fe_3GT we provide here a qualitative model that explains the experimental observation of antiferromagnetism in the quantum emitter

response. **Figure 5a** shows a schematic of the hysteresis curve with a decreasing sweep direction indicated by the blue line and an increasing sweep direction by the red line. As opposed to the hysteresis of ferromagnetic materials (Figure 4), the antiferromagnetic curve at 0 T does not remain magnetized. Therefore, we can divide the hysteresis curve into four parts: The decreasing field from positive magnetic field values to 0 (part 1), the decreasing field from 0 to negative fields (part 2), the increasing field from negative to 0 (part 3) and the increasing field from 0 to positive magnetic fields (part 4). Note that the experimentally determined energy splitting shown in **Fig. 3** was recorded along the same trajectory, which after an initial magnetization ramp was swept from positive magnetic fields to 0, then to a negative field, then back increasing from negative to positive. To illustrate the interplay between the two magnetic fields the blue arrows of the negative field range represent the magnetic dipole (μ) in FeGT that switches its orientation during the decreasing of the externally applied field (B). Similarly, the red arrows in the positive field range represent the magnetic dipole changing direction due to the increasing magnetic field. Region 1 and 3 represent the coupled case, where both the internal magnetic dipole of FeGT and the applied field point predominantly in the same direction. At 0 T the magnetic dipole and external field directions are opposite to each other, resulting in an uncoupled state. By increasing the magnetic field from 0 T the magnetic dipole starts shifting its orientation towards the coupled case, as shown in region 4. The same effect occurs by decreasing the field (region 2). This interplay between the internal and external fields leads to the characteristic behavior in the energy splitting ΔE in the optical emission from the quantum emitters in WSe_2, as illustrated in **Fig. 5b**.

Furthermore, one can use the response of the g factor of the quantum emitters in WSe_2 to determine the underlying magnetization in the FeGT material. In **Fig. 5a** of the 1st region, both the dipole and the field point predominantly in the same positive direction. This is a result of the coupling due to the proximity effect of quantum emitters in WSe_2 resulting in an enhancement of the g factor as compared to the uncoupled case. A similar effect occurs in region 3 where the negative dipole orientation and field direction also produce a proximity enhanced g factor. In contrast, for regions 2 and 4, the dipole and magnetic field are oriented in opposite direction (uncoupled case), and thus the quantum emitters in this area displays their normal exciton g factor that is not enhanced through a magnetic proximity effect. If one then considers the difference between the exciton g factor values determined at each magnetic field value from the increasing and decreasing field sweep, i.e. value of coupled case minus value of uncoupled case, one can reproduce the sine-like magnetization curve $\Delta M(B)$ shown in **Fig. 5c.** In this model, the maximum of the sine shaped magnetization curve relates to the saturation magnetization of the FeGT materials being probed through the local magnetic proximity effect, providing a qualitative model for the experimental response shown in **Figs. 3i** and **3f**.

Lastly, **Fig. 5d** provides statistical evidence for the proximity enhanced coupling with antiferromagnetic nature by recording magneto-PL measurements for 7 different quantum emitters, with 4 residing on the Fe_3GT/WSe_2 sample and 3 emitters on the Fe_5GT/WSe_2 sample. See **Supplementary Table 1** for details of the parameters. Here the antiferromagnetic coupling strength is analyzed from the swing ΔM defined as the difference between the highest positive value and highest negative value in the sine-shaped curves (**Fig. 3i**). For all observed quantum emitters, the average swing ΔM is pronounced with values ranging from 130-240 μeV. As a result, our all-optical read out technique can sense the magnetization in the partially oxidized Fe_3GT and Fe_5GT layers through highly spatially localized quantum emitters, without the need for electrodes that are required for electric transport measurements.

Conclusions

We have utilized strain-induced quantum emitters to probe for magnetic proximity coupling in vdW heterostructures. The spectrally narrow spin-doublet of the WSe_2 quantum emitters allowed to fully resolve the hysteretic magneto-response in the exciton emission, revealing the characteristic signatures of ferromagnetic and antiferromagnetic proximity coupling. Combined with the well-known surface oxidization of the Fe containing vdW crystals, the antiferromagnetic response originates in the interplay between Fe_3GT or Fe_5GT, a thin O-Fe_3GT layer, and the spin doublets of the quantum emitters. These findings support a qualitative model that highlights the underlying switching between coupled and uncoupled spin orientations between the quantum emitters and the antiferromagnetic vdW layers, depending on the external magnetic field strength and direction. Our work highlights the utility of 0D quantum emitters for probing local magnetic fields, hysteresis effects, and interface magnetic dipoles in vdW heterostructures with high precision. The observation of hard-ferromagnetic response directly in the optical emission of strongly localized 0D excitons adds also new degrees for spin and g-factor manipulation of quantum states, that find application in quantum information processing. Particularly, the demonstrated case for samples made under a glove box is appealing, since spin quantum state manipulation can now be carried out directly on-chip through proximity-coupling with vdW ferromagnets and in the absence of external magnetic fields from bulky superconducting coils. When combined in future work with gate-controlled hard-ferromagnetism of vdW materials, dynamic and reversible on-chip manipulation of magneto-optical properties of quantum emitters might be even realized, which would constitute a significant step in scaling up on-chip spin quantum systems.

Methods

Sample Preparation and stamping procedure: The vdW ferromagnetic materials CGT, Fe_3GT and Fe_5GT were mechanically exfoliated down to few-layer thin films from commercial crystals (HQ graphene). Monolayers of WSe_2 were exfoliated either from commercial crystals grown by CVT (HQ Graphene) or from bulk crystals grown by the flux-growth technique, giving rise to a one to two orders of magnitude lower defect density and a higher emission PL intensity, as we previously reported [36]. In order to produce nanobubbles as seen in the data from Figure 2, we used the cold stamping process[40]. Before the transfer, surface cleaning was done through submerging the SiO_2 substrate in 30% KOH solution for 15 min and rinsed in DI water for 3 min. Cold-Stamping was done immediately after surface preparations were completed. The transfer process was carried out by hard pressing at room-temperature, with the ferromagnetic material layer stamped down first followed immediately by stamping of the WSe_2 monolayer flake. The entire assembly process of the heterostructures was carried out in air. Fe containing samples were typically exposed for 30-60 min to air during which time the native oxide forms.

Optical measurements: Photoluminescence measurements were performed at 3.5 K using a closed-cycle cryogen-free cryostat (attoDRY 1100, attocube systems AG). For optical excitation, we used a laser diode operating at 532 nm in continuous-wave mode. A laser spot size of ~0.85 μm was achieved using a cryogenic microscope objective with a numerical aperture of 0.82. The relative position between the sample and the laser spot was adjusted with a cryogenic piezoelectric xyz stepper, whereas 2D scanned images were recorded with a cryogenic 2D-piezo scanner (Attocube). The spectral emission from the sample was collected in a multimode fiber, dispersed using a 0.75 m focal length spectrometer with either a 300 or 1200 groove grating, and imaged by a liquid nitrogen-cooled silicon charge coupled device (CCD) camera. Magnetic fields were applied perpendicular to the plane of the sample within the range of -9 T to +9 T.

Atomic Force Microscope (AFM) Imaging: The AFM measurements in **Fig. S1** were obtained using a Bruker Dimension FastScan AFM in noncontact mode at a scan speed of 1Hz with a FastScan-B tip that has a nominal spring constant of 1.8 N m^{-1}. The AFM height profiles were extracted from the images using Gwyddion open-source software.

Conflicts of interest

There are no conflicts to declare

Acknowledgments

Primary support for this work was provided by the National Science Foundation (NSF) under award DMR-1809235 (Stevens Institute of Technology) and DMR-1809361 (Columbia University), CAREER DMR-1553788 (University of Rochester) and AFOSR FA9550-19-1-0074 (University of Rochester). Synthesis of WSe_2 crystals was supported by the NSF MRSEC program through Columbia in the Center for Precision Assembly of Superstratic and Superatomic Solids (DMR-1420634). S.S. acknowledges financial support for the attodry1100 under NSF award ECCS-MRI-1531237.

References

[1] Burch, K.S.; Mandrus, D.; Park, J.G. Magnetism in Two-dimensional Van der Waals Materials, *Nature*, **2018**, 563, 47-52.

[2] Gibertini, M.; Koperski, M.; Morpurgo, A.F.; Novoselov, K.S. Magnetic 2D Materials and Heterostructures, *Nat. Nanotechnol.* **2019**, 14, 408-419.

[3] Gong, C.; Zhang, X.; Two-dimensional Magnetic Crystals and Emergent Heterostructure Devices, *Science*, **2019**, 363, 706.

[4] Albarakati, S.; Tan, C.; Chen, Z.J. et al; Antisymmetric Magnetoresistance in van der Waals Fe_3GeTe_2/graphite/Fe_3GeTe_2 Trilayer Heterostructures, *Sci. Adv.* **2019**, 5, eaaw0409.

[5] Zollner, K.; Junior, P.E.F.; Fabian, J.; Proximity Exchange Effects in $MoSe_2$ and WSe_2 Heterostructures with CrI_3: Twist Angle, Layer, and Gate Dependence, *Phys. Rev. B* **2019**, 100, 085128.

[6] Wang, Z.; Sapkota, D.; Taniguchi, T.; Watanabe, K.; Mandrus, D.; Morpurgo, A.F.; Tunneling spin Valves Based on Fe_3GeTe_2/hBN/Fe_3GeTe_2 van der Waals Heterostructures, *Nano Lett.* **2018**, 18, 4303-4308.

[7] Aiv Aivazian, G.; Gong, Z.; Jones, A. M.; Chu, R. L.; Yan, J.; Mandrus, D. G.; Zhang, C.; Cobden, D.; Yao, W.; Xu, X. Magnetic Control of Valley Pseudospin in Monolayer WSe_2. Nat. Phys. **2015**, 11, 148−152.

[8] MacNeill, D.; Heikes, C.; Mak, K. F.; Anderson, Z.; Kormányos, A.; Zólyomi, V.; Park, J.; Ralph, D. C. Breaking of Valley Degeneracy by Magnetic Field in Monolayer $MoSe_2$. *Phys. Rev. Lett.* **2015**, 114, 037401.

[9] Cao, T.; Wang, G.; Han, W.; Ye, H.; Zhu, C.; Shi, J.; Niu, Q.; Tan, P.; Wang, E.; Liu, B.; Feng, J. Valley-Selective Circular Dichroism of Monolayer Molybdenum Disulphide. *Nat. Commun.* **2012**, 3, 887.

[10] Zhao, C.; Norden, T; Zhang, P.; Zhao, P.; Cheng, Y.; Sun, F.; Parry, J.P. et al; Enhanced Valley Splitting in Monolayer WSe_2 due to Magnetic Exchange Field. *Nat. Nanotechnol.* **2017**, 12, 757-762.

[11] Zhang, Q.; Yang, S.A.; Mi, W.; Cheng, Y.; Schwingenschlogl, U. Large Spin-Valley Polarization in Monolayer $MoTe_2$ on Top of EuO(111). *Adv. Mater.* **2016**, 28, 959-966.

[12] Zhong, D.; Seyler, K.L. et al; Van der Waals Engineering of Ferromagnetic Semiconductor Heterostructures for Spin and Valleytronics, *Sci. Adv.* **2017**, 3, e1603113.

[13] Huang, B.; Clark, G.; Navarro-Moratalla, E.; Klein, D.R.; Cheng, R.; Seyler, K. L.; Zhong, D.; Schmidgall, E.; Mcguire, M.A.; Cobden, D.H.; Yao, W.; Xiao, D.; Jarillo-Herrero, P.; Xu, X. Layer-dependent Ferrimagnetism in a Van der Waals Crystal Down to the Monolayer Limit, *Nature*, **2017**, 546, 270-273.

[14] Tan, C.; Lee, J.; Jung, S.; Park, T.; Albarakati, S.; Partridge, J.; Field. M. R.; McCulloch, D. G.; Wang, L.; Lee, C. Hard Magnetic Properties in Nanoflake Van Der Waals Fe_3GeTe_2. *Nat. Commun.* **2018**, 9, 1554.

[15] May, A.F.; Calder, S.; Cantoni, C.; Cao, H.; Mcguire, M.A.; Magnetic Structure and Phase Stability of the van der Waals Bonded Ferromagnet $Fe_{3-x}GeTe_2$, *Phys. Rev. Lett.* **2016**, 93, 014411.

[16] Verchenko, V.Y.; Tsirlin, A.A.; Sovolev, A.V.; Presniakov, I.A.; Shevelkov, A.V.; Ferromagnetic Order, Strong Magnetocrystalline Anisotropy, and Magnetocaloric Effect in the Layered Telluride $Fe_{3-\delta}GeTe_2$. *Inorg. Chem.* **2015**, 54, 8598-8607.

[17] Deng, Y.;Yu, Y.;Song, Y.;Zhang, J.; Wang, N. Z.;Sun, Z.; Yi, Y.; Wu, Y.Z.; Wu, S.; Zhu, J.; Wang, J.; Chen, X. H.; Zhang, Y. Gate Tunable Room-Temperature Ferromagnetism in Two-Dimensional Fe_3GeTe_2. *Nature* **2018**, 563, 94-99.

[18] Jiang, S.; Shan, J.; Mak, K. F.; Electric field Switching of Two-dimensional Van der Waals Magnets, *Nature Mater.* **2018**, 17, 406-410.

[19] Klein, D.R.; MacNeill, D.; Lado, J.L.; Soriano, D. Navarro-Moratalla, E.; Watanabe, K.; Taniguchi, T.; Manni, S.; Canfield, P.; Fernandez-Rossier, J.; Jarillo-Herrero, P. Probing Magnetism in 2D van der Waals Crystalline insulators via electron tunneling, *Science*, **2018**, 360, 1218-1222.

[20] Sun, Z.; Yi, Y.; Song, T.; Clark, G.; Huang, B.; Shan, Y.; Wu, S.; Huang, D.; Gao, C.; Chen, Z.; Mcguire, M.; Cao, T.; Xiao, D.; Liu, W.T.; Yao, W.; Xu, X.; Wu, S.; Giant Nonreciprocal Second-harmonic generation from antiferromagnetic bilayer CrI_3, *Nature*, **2019**, 572, 497-501.

[21] Gong, C.; Li, L.; Li, Z.; Ji, H.; Stern, A.; Xia, Y.; Cao, T.; Bao, W.; Wang, C.; Wang, Y.; et al. Discovery of Intrinsic Ferromagnetism in Two-Dimensional van der Waals Crystals. *Nature* **2017**, 546, 265−269.

[22] Fei, Z.; Huang, B.; Malinowski, P.; Wang, W.; Song, T.; Sanchez, J.; Yao, W.; Xiao, D.; Zhu, X.; May, A.F.; Wu, W.; Cobden, D.H.; Chu, J. H.; Xu, X.; Two-dimensional Itinerant Ferromagnetism in Atomically Thin Fe_3GeTe_2. *Nature Mater.* **2018**, 17, 778-782.

[23] Ji, H.; Stokes, R.A.; Alegria, L.D.; Blomberg, E.C.; Tanatar, M.A.; Reijnders. A.; Schoop, L.M.; Liang, T.; Prozorov, R.; Burch, K.S.; Ong, N.P.; Petta, J.R.; Cava, R.J. A Ferromagnetic Insulating Subatrate for the Epitaxial Growth of Topological Insulators, *J. Appl. Phys.* **2013**, 111, 114907.

[24] Deiseroth, H. J.; Aleksandrov, K.; Reiner, C.; Kienle, L.; Kremer, R.K. Fe_3GeTe_2 and Ni_3GeTe_2-Two New Layered Transition-Metal Compounds: Crystal Structures, HRTEM Investigations, and Magnetic and Electrical Properties. *Eur. J. Inorg. Chem.* **2006**,1561-1567.

[25] Leon-Brito, N.; Bauer, E. D.; Ronning, F. Thompson, J. D.; Movshovish, R. Magnetic Microstructure and Magnetic Properties of Uniaxial Itinerant Ferromagnet Fe_3GeTe_2. *J. Appl. Phys.* **2016**, 120, 083903.

[26] Li, Q.; Yang. M.; Gong, C.; Chopdekar, R.V.; Ndiaye, A.T. Turner, J.; Chen, G.; Scholl, A.; Shafer, P.; Arenholz, E.; Schmid, A.K.; Wang, S.; Liu, K.; Gao, N.; Admasu, A.S.; Cheong, S.W.; Hwang, C.; Li, J.; Wang, F.; Zhang, X.; Qiu, Z. Patterning-Induced Ferromagnetism of Fe_3GeTe_2 Van der Waals Materials Beyond Room Temperature. *Nano Lett*. **2018**, 18, 5974-5980.

[27] Stahl, J.; Shlaen, E.; Johrendt, D. The Van Der Waals Ferromagnets $Fe_{5-\delta}GeTe_2$ and $Fe_{5-\delta-x}Ni_xGeTe_2$-Crystal Structure, Stacking Faults, and magnetic Properties. *Z. Anorg. Allg. Chem.* **2018**, 644, 1923-1929.

[28] May. A. F.; Ovchinnikov, D.; Zheng, Q.; Hermann, Eaphael.; Hermann, R.; Calder, S.; Huang, B.; Fei, Z.; Liu, Y. Xu, X.; Mcguire, M.A. Ferromagnetism Near room Temperature in the Cleavable van der Waals Crystal Fe_5GeTe_2. *ACS Nano* **2019**, 13, 4436-4442.

[29] Kim, D.; Park, S.; Lee, J.; Yoon, J.; Joo, S.; Kim, T.; Min, K.; Park, S.; Kim, C.; Moon, K.; Lee, C.; Hong, J.; Hwang, C. antiferromagnetic Coupling of Van der Waals Ferromagnetic Fe_3GeTe_2. *Nanotechnology*, **2019**, 30. 245701.

[30] Jungwirth, T.; Marti, X.; Wadley, P.; Wunderlich, J.; Antiferromagnetic Spintronics, *Nat. Nanotechnol.* **2018**, 11, 231-241.

[31] Wadley, P.; Howells, B.; Zelezny, J.; Andrew, C.; Hills, V.; Campion, R.P.; Novak, V.; Olejnik, K.; Maccherozzi, F.; Dhesi, S.S.; Electrical Switching of an Antiferromagnet, *Science*, **2016**, 351, 587-590.

[32] Dolui, K.; Petrovic, M.D.; Zollner, K.; Plechac, P.; Fabian, J.; Nicolic, B.K.; Proximity Spin-Orbit Torque on a Two-Dimensional Magnet within van der Waals Heterostructure: Current-Driven Antiferromagnet-to-Ferromagnet Reversible Nonequilibrium Phase Transition in Bilayer CrI_3, *Nano Lett.* **2020**, 20, 2288-2295.

[33] Zhong, D.; Seyler, K.L.; Linpeng, X.; Wilson, N.P.; Taniguchi, T.; Watanabe, K.; Mcguire, M.A.; Fu, K.C.; Xiao, D.; Yao, W.; Xu, X.D.; Layer-resolved Magnetic Proximity Effect in van der Waals Heterostructures, *Nat. Nanotechnol.* **2020**, 15, 187-191.

[34] Chen, B.; Xu, H.; Ma, C.; Mattauch, S.; Lan. D.; Jin, F.; Guo, Z.; Wan, S.; Chen, P.; Gao, G.; Chen, F.; Su, F.; Wu, W. All-oxide-based Synthetic Antiferromagnets Exhibiting Layer-resolved Magnetization Reversal. *Science* **2017**, 357, 191-194.

[35] Fu, S.; Kang, K.; Shayan, K.; Yoshimura, A.; Dadras, S.; Wang, X.; Zhang, L.; Chen, S.; Liu, N.; Jindal, A.; Li, X.; Pasupathy, A.N.; Vamivakas, A.N.; Menuier, V.; Strauf, S.; Yang, E.H.; Enabling Room Temperature Ferromagnetism in Monolayer MoS_2 via in situ iron-doping. *Nat. Commun.* **2020**, 11, 2034.

[36] Shayan, K.; Liu, N.; Cupo, A.; Ma, Y.; Luo, Y.; Meunier, V.; Strauf, S. Magnetic Proximity Coupling of Quantum Emitters in WSe_2 to Van der Waals Ferromagnets, *Nano Lett.* **2019**, 19,7301-7308

[37] He, J.; Ding, G.; Zhong, C.; Li, S.; Li, D.; Zhang, G. Remarkably Enhanced Ferromagnetism in Super Exchange Governed $Cr_2Ge_2Te_6$ Monolayer via Molecular Adsorption. *J. Mater. Chem. C* **2019**, 7, 5084-5093.

[38] Zhuang, H. L.; Kent, P R.C.; Hennig, R. G.; Strong Anisotropy and Magnetostriction in the Two-Dimensional Stoner Ferromagnet Fe_3GeTe_2. *Phys. Rev. B* **2016**, 93, 134407.

[39] Joe, M.; Yang, U.; Lee, C.; First-principles Study of Ferromagnetic Metal Fe_5GeTe_2, *Nano Materials Science* **2019**, 1, 299-303.

[40] Shepard, G. D.; Ajayi, O. A.; Li, X. Z.; Zhu, X. Y.; Hone, J. Strauf. S. Nanobubble Induced Formation of Quantum Emitters in Monolayer Semiconductors. *2D Mater.* **2017**, 4, 021019.

[41] Luo, Y.; Deterministic Coupling of Site-controlled Quantum Emitters in Monolayer WSe_2 to Plasmonic Nanocavites, *Nature Nano.* **2018**, 13, 1137-1142.

[42] Luo, Y.; Liu, N.; Kim, B.; Hone, J.; Strauf, S.; Exciton dipole orientation of strain-induced quantum emitters in WSe_2, *Nano Lett.* **2020**, *20*, 5119-5126.

[43] Kumar, S.; Kaczmarczyk, A.; Gerardot, B. D. Strain-Induced Spatial and Spectral Isolation of Quantum Emitters in Mono-and Bilayer WSe_2. *Nano Lett.* **2015**, 15, 7567−7573.

[44] Linhart, L.; Paur, M.; Smejkal, V.; Burgdorfer, J.; Mueller, T.; Libisch, F. Localized Intervalley Defect Excitons as Single-Photon Emitters in WSe_2. *Phys. Rev. Lett.* **2019**, 123, 1465401.

[45] Zhu, J.X.; Janoschek, M.; Chaves, D.S.; Cezar, J.C.; Durakiewicz, T.; Ronning, F.; Sassa, Y.; Mansson, M.; Scott, B.L.; Wakeham, N.; Bauer, E.D.; Thompson, J.D. Electronic Correlation and Magnetism in the Ferromagnetic Metal Fe_3GeTe_2, . *Phys. Rev. B* **2016**, 93, 144404.

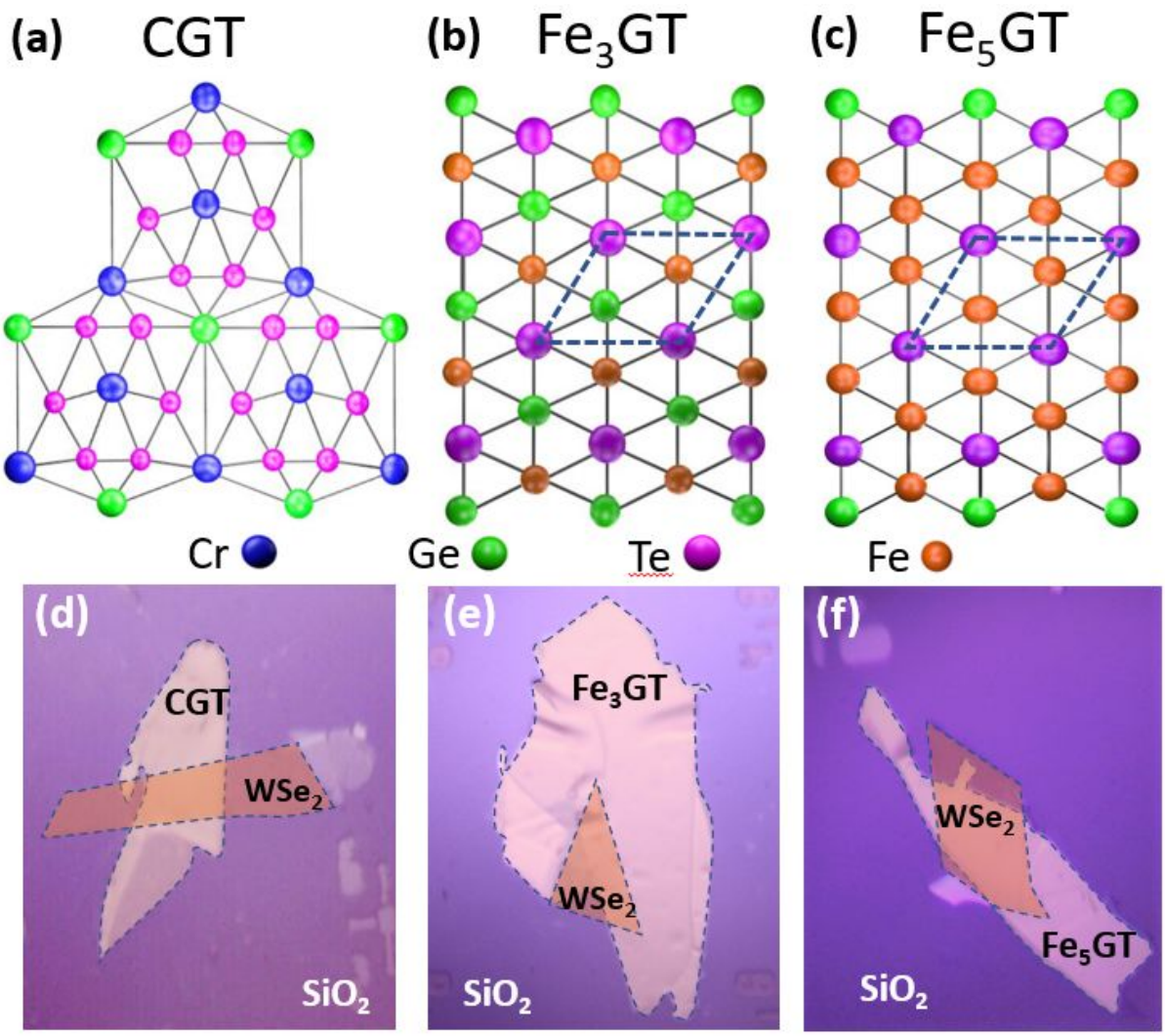

Figure 1 Formation of heterostructures of WSe_2 monolayer with hard and soft van der Waals ferromagnetic materials. (a-c) Top views of the crystal structure for the soft ferromagnet CGT (a), the hard ferromagnet Fe_3GT (b), and Fe_5GT (c). The unit cell is enclosed by the dotted line. (d-f) Corresponding optical-microscope images of an assembled CGT/WSe_2 heterostructure (d), an Fe_3GT/WSe_2 heterostructure (e) and an Fe_5GT/WSe_2 heterostructure (f). The boundary of the ferromagnetic and semiconducting crystals are outlined by the dotted lines.

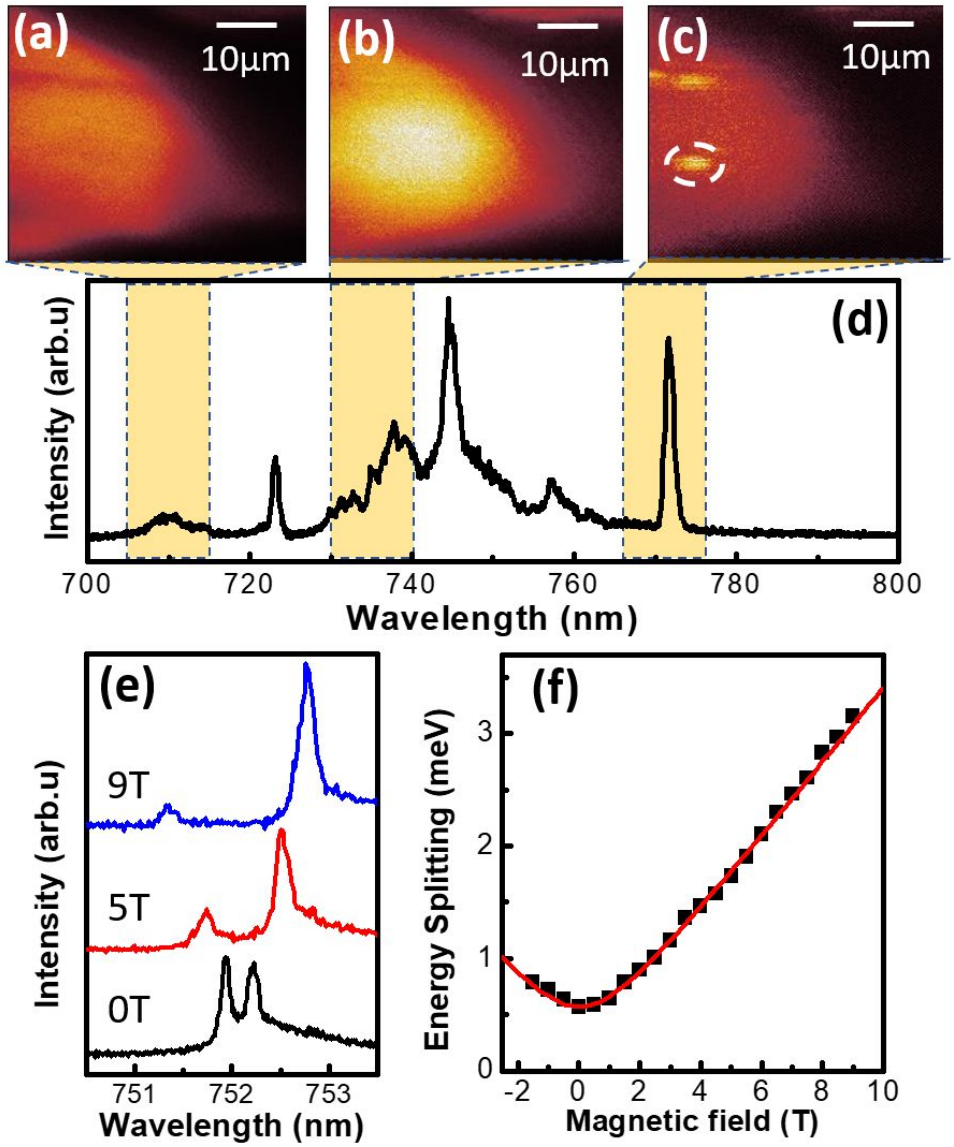

Figure 2 Magneto-optical characterization of quantum emitters in Fe_3GT/WSe_2 heterostructures. Hyperspectral PL images of WSe_2 monolayer recorded by bandpass filters centered at 710 nm (a), 730 nm (b) and 770 nm (c), respectively. Band width: 10 nm. Note the Fe_3GT layer is not visible in the image since it does not emit light. (d) Corresponding PL spectrum, highlighting the filter settings. (e) Magnetic field dependence of an exemplary quantum emitter similar to the one highlighted by the hot spot in figure (c). (f) Corresponding Zeeman Energy splitting as a function of magnetic field. The solid line is a fit to the standard relation given in the text to determine the g-factor. All data recorded at 3.5 K.

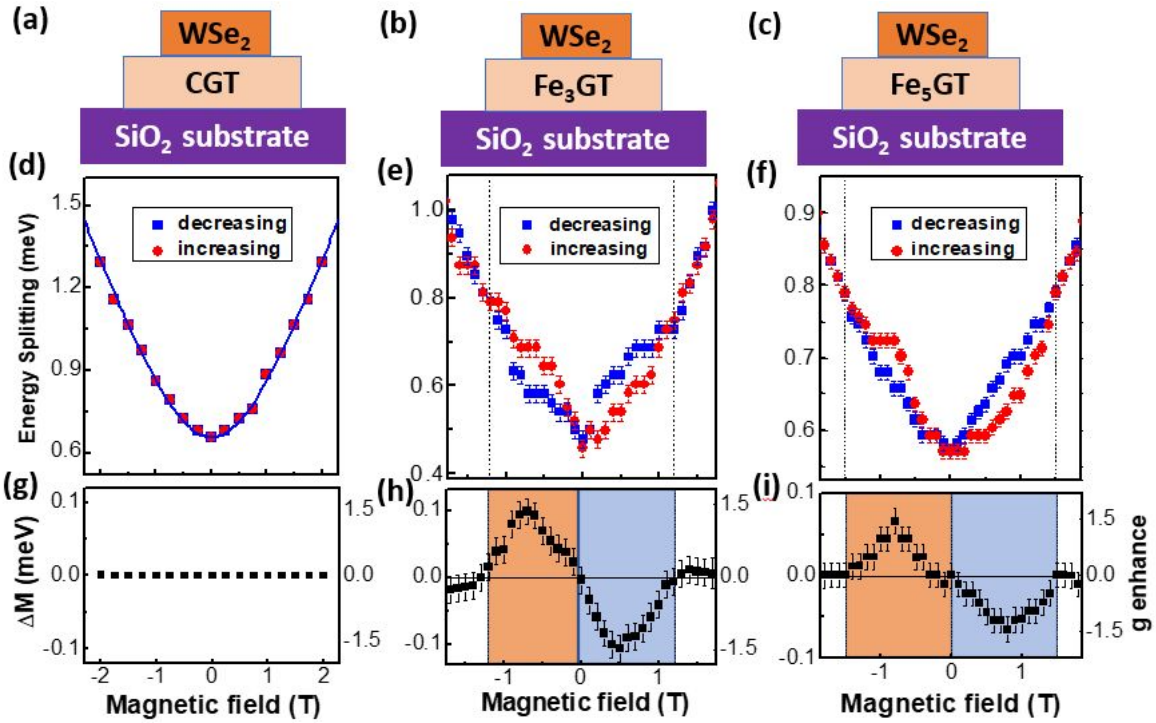

Figure 3 Magnetic hysteresis measurements probed via the Zeeman splitting of the quantum emitter residing in WSe_2. Schematic of the layer stacking sequence of CGT/WSe_2 (a), Fe_3GT/WSe_2 (b) and Fe_5GT/WSe_2 (c), respectively. Zeeman energy splitting as a function of increasing (red circles) and decreasing (blue square) magnetic field for quantum emitters residing in CGT/WSe_2 (d), Fe_3GT/WSe_2 (e) and Fe_5GT/WSe_2 (f) heterostructures. Corresponding energy difference ΔM and g factor enhancement between increasing and decreasing magnetic field for quantum emitters residing in CGT/WSe_2 (g), Fe_3GT/WSe_2 (h) and Fe_5GT/WSe_2 (i) heterostructures. All data recorded at 3.5 K.

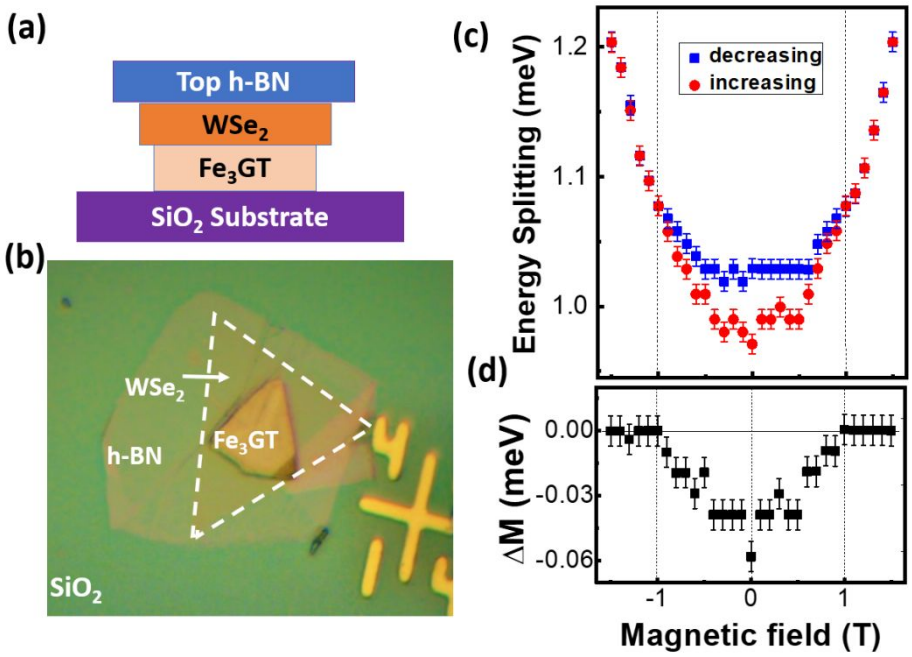

Figure 4 Probing proximity-induced hysteresis in the absence of native oxides. (a) Schematic of layer stacking sequence for the Fe_3GT/WSe_2 heterostructure made under glove box conditions. (b) Corresponding optical-microscope image. The WSe_2 boundary is outlined by the dotted line. (c) Zeeman energy splitting of a quantum emitter as a function of increasing (red circles) and decreasing (blue square) magnetic field. (d) Corresponding energy difference ΔM between increasing and decreasing magnetic field. All data recorded at 3.5K.

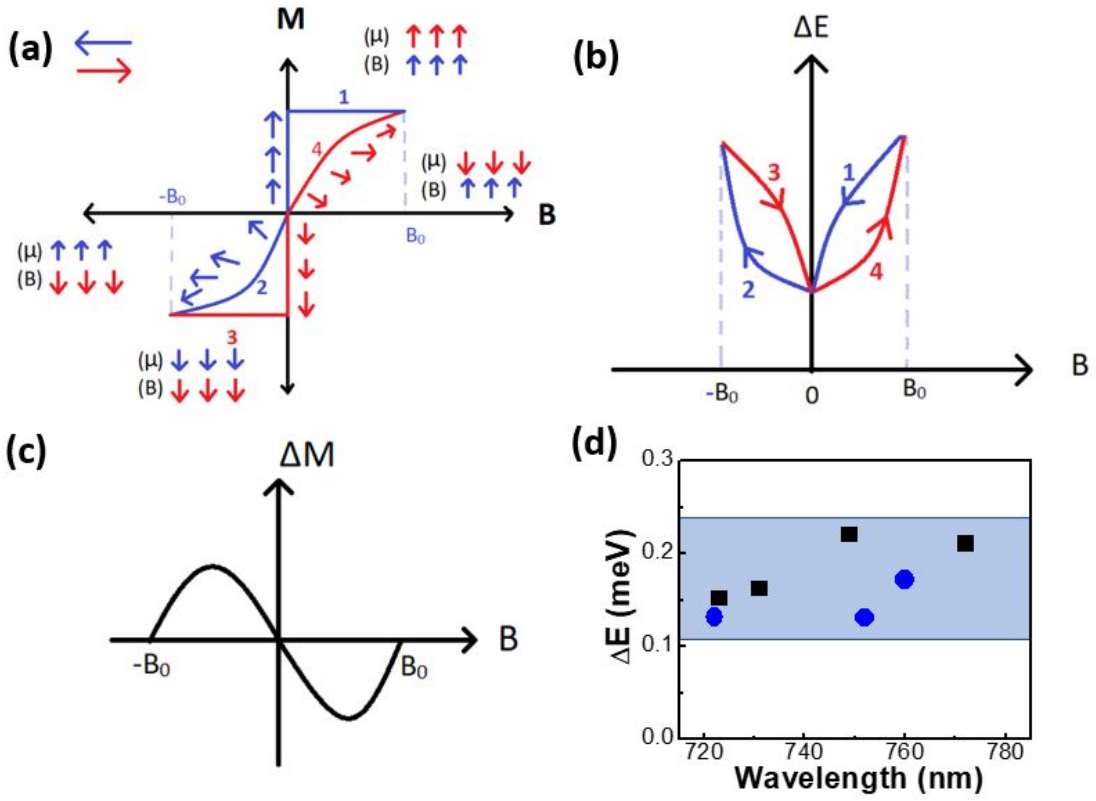

Figure 5 Qualitative model of antiferromagnetic proximity coupling and statistical evidence from 7 quantum emitters. (a) Theoretical model of magnetization of FeGT with decreasing (blue) and increasing (red) magnetic field. (b) Corresponding Zeeman energy splitting of the quantum emitter with decreasing (blue) and increasing (red) magnetic field. (c) Corresponding energy difference ΔM between increasing and decreasing magnetic field showing asymmetric response. (d) Swing of ΔM recorded for 7 quantum emitters. Black squares are for emitters residing in heterostructures with Fe_3GT and blue circles for emitters in Fe_5GT that were immediately recorded after fabrication. All data recorded at 3.5 K.